Microfluid Nanofluid (2016) 20:16
DOI 10.1007/s10404-015-1691-0

RESEARCH PAPER

Hydrodynamically controlled cell rotation in an electroporation microchip to circumferentially deliver molecules into single cells

Mingde Zheng[1] · Jerry W. Shan[2] · Hao Lin[2] · David I. Shreiber[1] · Jeffrey D. Zahn[1]

Received: 14 August 2015 / Accepted: 13 December 2015 / Published online: 7 January 2016

Abstract We present a hydrodynamically controlled, single-cell-rotation method to demonstrate electroporation-mediated molecular delivery in a microfluidic channel. Using a two-inlet geometry to control the carrier-flow profile, cell flow path and angular velocities can be controlled. When the flow-rate ratio between the fluid sheath and cell streams is balanced, fluidic shear occurs near the walls of the channel due to differential flow velocities between the streamlines. Single-cell angular velocities can then be explicitly controlled by using higher flow-rate ratios between the streams. Using sheathing streams with sufficiently high flow-rate ratios between the sheath and sample streams, cells are pinched against the sidewalls of the channel, which results in large degrees of cell rotation. We applied this technique to single-cell electroporation to increase the delivery of small molecules into the cell. Cell orientation was controlled along the length of the microchannel to continuously expose new cell membrane surface area to an applied electric field. Thus, the cell membrane becomes circumferentially permeabilized, resulting in a more efficient and uniform transport of micro- and macromolecules into rotating cells compared to the non-rotating one. Hydrodynamic control of cell rotation offers a new means to enhance intracellular delivery efficiency in single-cell electroporation.

Keywords Single-cell manipulation · Cell rotation · Microfluidics · Electroporation · Molecular transport · Electrokinetics

1 Introduction

Transfection is a powerful tool that has been used extensively in the life sciences to investigate gene and gene product functions. It has contributed to the advancement of basic cellular research, drug discovery and target validation (Kim and Eberwine 2010). Electroporation is one of the well-established transfection techniques that is commonly used to introduce a wide range of molecules such as drugs, DNA, plasmids or proteins into cells. Electroporation is typically performed by exposing cells to an electric field of sufficient strength to transiently permeabilize the cell membrane, then allowing it to reseal after the field is removed. Emerging applications of electroporation can be found in cancer treatment, gene therapy, transdermal drug delivery and stem cell research (Mir 2000; Gehl 2003).

Electroporation has been commonly used on the macroscale to transfect millions of cells at once. However, this approach involves exposing the cells to a non-uniform electric field and variable pH near electrodes, which can lead to heterogeneous delivery and often low cell viability, even in commercial systems with specialized cuvettes (Khine et al. 2007; Kim et al. 2008). These issues can be minimized by applying electric fields at the microscale, thereby enabling

Electronic supplementary material The online version of this article (doi:10.1007/s10404-015-1691-0) contains supplementary material, which is available to authorized users.

✉ Mingde Zheng
jmzheng@rutgers.edu

✉ Jeffrey D. Zahn
jdzahn@rci.rutgers.edu

[1] Department of Biomedical Engineering, Rutgers, The State University of New Jersey, 599 Taylor Road, Piscataway, NJ 08854, USA

[2] Department of Mechanical and Aerospace Engineering, Rutgers, The State University of New Jersey, 98 Brett Road, Piscataway, NJ 08854, USA

more consistent delivery efficiency and cell viability. Microscale electroporation potentially allows other advantages, including: (1) in situ visualization of the molecular delivery process, (2) continuous and real-time tracking of cellular response to electroporation, and (3) electroporation and delivery to individual cells (Golzio et al. 2002; Khine et al. 2005; Kim et al. 2007; Lee et al. 2008; Kim et al. 2008).

Successful electroporation for cell transfection depends on the transport and accumulation of molecules in a permeabilized cell, maximizing delivery while limiting excessive permeability that can lead to cell death. We have previously used numerical simulations and experimental validation to elucidate the physical principles behind electroporation-mediated molecular uptake (Li and Lin 2011; Li et al. 2013; Sadik et al. 2013b; Demiryurek et al. 2015). Due to the polar phenomena of electroporation, only the membrane surface perpendicular to the electric field becomes permeabilized once the transmembrane potential threshold is reached. Since the accumulation of charged molecules during electroporation also occurs at the polar region of the cell membrane, the amount of material delivered to the porated site can become saturated, limiting further delivery into the cell. We hypothesize that, by rotating the cell during the application of a permeabilizing electric field, a larger portion of the cell membrane area could be exposed and electroporated to allow for greater total delivery into the cell, and the delivered molecules would be more uniformly distributed circumferentially inside the cell.

Although many single-cell manipulation techniques exist to physically transport, sort, trap and fuse biological cells (Andersson and van den Berg 2003; Dittrich and Manz 2006; Yun et al. 2013), there are limited reports on controlling the rotation of single cells. Dielectrophoresis (DEP) has been used to capture and orient single cells at the microscale (Schnelle et al. 2000; Jons 2003). Daniel Chiu and colleagues created microvortices from diamond-shaped chambers adjacent to the flow channel to hydrodynamically circulate trapped cells (Shelby and Chiu 2004; Chiu 2007). Methods that utilize only hydrodynamic flow are perhaps the simplest and most harmless approaches to control cell rotation (Pamme 2007; Di Carlo et al. 2007; Hur et al. 2011). By using stratified flows in the microfluidic channel and varying the respective flow rates and ratios between each infused stream, flowing single cells are not only able to be positioned anywhere across the width of the microchannel, but their orientation and rotation rate along the channel sidewall can be controlled as well. One particular example of controlling cell positioning found in the literature is the pinched-flow fractionation of particles in microchannels demonstrated by Yamada and colleagues (Yamada et al. 2004; Takagi et al. 2005). By applying a fluid sheathing flow to align particles of different sizes to the sidewall of a pinched microchannel segment, particles can be separated by size as their centroids are at varying positions from the sidewall and follow different paths based on a spreading flow profile at a downstream expansion within the microchannel. However, this approach did not explicitly examine particle rotation when they were pinched to the sidewall. In this work, we adapt the pinch flow technique to position cells against a channel sidewall while exploring how this leads to reproducible particle rotation rates. Because cell rotation exposes a larger, changing cell surface area to a perpendicular electric field, we demonstrate how combining microscale electroporation with rotating cells can facilitate intracellular molecular delivery.

2 Materials and methodology

2.1 Microfabrication

Microfluidic channels with a two-inlet, two-outlet and a three-inlet, three-outlet geometry were designed in AutoCad designer software (Autocad 2015, Autodesk, San Rafael, CA) with a dimension of 1 cm in length, 150 μm in width, and 20 μm in depth. Microchannels were fabricated using standard soft lithography methods from an SU-8-based master mold. Briefly, a ratio of 1:10 polydimethylsiloxane (PDMS) elastomer to curing agent was mixed then cast onto the master mold to obtain a negative replica of the features after overnight oven curing at 65°C. In order to fabricate planar electrodes, a physical-vapor-deposition machine (PVD75, Kurt & Lesker, Jefferson Hills, PA) was used to sputter titanium (~1000 Å) and platinum (~3000 Å) onto lithographically patterned and hydrofluoric-acid-etched glass substrates, followed by photoresist dissolution in acetone in a lift-off process. The electrodes are defined as a pair of metal traces 50 μm in width with a center-to-center spacing of 410 μm between each trace. This distance allows sufficient cell transit time in between the electrodes while applying the predefined electroporation pulse without generating electrolysis. To complete the electrode-embedded microfluidic device, the surfaces of the PDMS microfluidic device and the glass substrate with patterned electrodes were treated under oxygen plasma at 100 W power, 250 sccm O_2 at 700 mTorr for 60 s. Immediately following surface activation, the electrodes were aligned and bonded with the PDMS microfluidic channel under a stereo microscope (Olympus SZ61, Center Valley, PA) to create a vertical intersect of the microfluidic channel (Fig. 1). Conductive epoxy (Circuit Works, Inc, Somerville, NJ) was then used to fuse the exposed planar electrode pads with copper wires, allowing connection with external electronics.

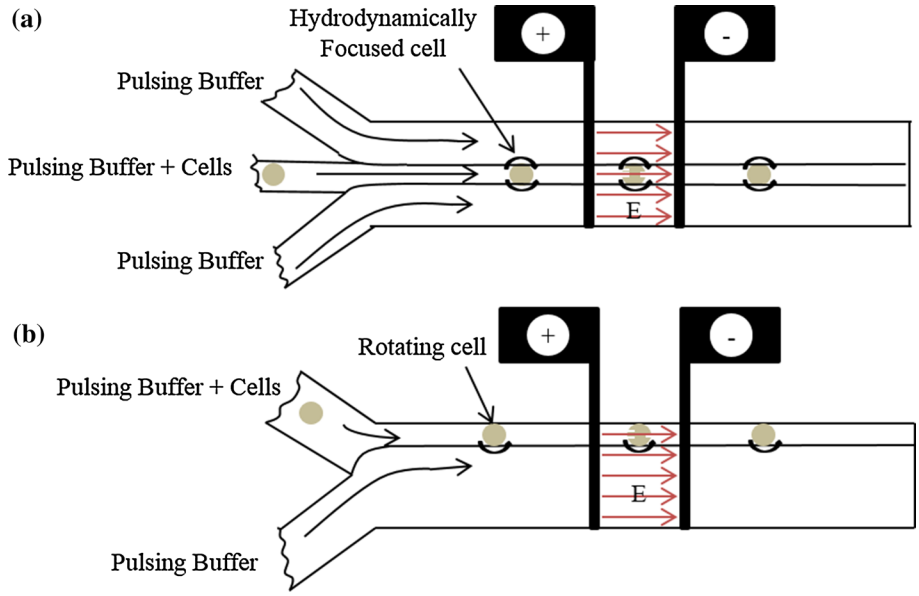

Fig. 1 **a** Schematic of a three-inlet microchannel with cell carrier flow being hydrodynamically focused between two sheathing flows. **b** Schematic of a two-inlet microchannel with electroporating electrodes across the channel. The cell carrier buffer is infused from the *top inlet*, whereas the sheath pulsing buffer is infused from the *bottom* to pinch the cells into a single file along the sidewall

2.2 Microelectroporation

To enable fluorescence-based delivery monitoring during the experiment, propidium iodide (PI) was added to the pulsing buffer at a final solution concentration of 100 µM. PI (P3566, Life Technologies, Grand Island, NY) is a dye that fluoresces upon binding to nucleic acids, with an excitation wavelength of 536 nm and emission wavelength of 617 nm. It is membrane impermeant and cannot enter a cell unless the cell membrane is compromised, and therefore, it is used as a label to track cell permeability following electroporation. A fluorescein-conjugated dextran (FD) with a molecular weight of 10 kDa (D-1821, Life Technologies, Grand Island, NY) was also used for intracellular delivery of large molecules. FD (494 nm excitation, 524 nm emission) was separately added into the cell buffer at 100 µM during the continuous electroporation experiments. A custom-designed electroporator was used to conduct all electroporation procedures (Sadik et al. 2013b). It consists of a DC power supply (KiKusui Pan70-5A, Yokohama, Japan) and high voltage (350 volts), high capacitance (2100 µF), electrolytic capacitors (Capitol Scientific, Austin, TX) for storing sufficient electric charge, and an electronics module for voltage adjustment, external triggering, and multiple-pulse application. A pulse delay generator (BNC-555, Berkeley Nucleonics Corporation, San Rafael, CA) was used to control the pulse duration, delay and frequency of application.

2.3 Cell culture

NIH 3T3 mouse fibroblasts were cultured in Dulbecco's modified Eagle's medium supplemented with 10 % v/v fetal bovine serum, 1 % v/v penicillin–streptomycin and 1 % L-glutamine (Sigma-Aldrich, St. Louis, MO). Cells were cultured to ~80 % confluency before being harvested for experiments. An average diameter of 10 µm was found for the suspended cells. Prior to each experiment, the cells were trypsinized for 2 min and resuspended in an electroporation buffer following centrifugation and aspiration of the trypsin media. The electroporation buffer (hereafter referred to as the pulsing buffer) is an iso-osmotic solution consisting of 250 mM sucrose, 10 mM HEPES and 0.4 mM of M_gCl_2 salt to provide a buffer conductivity of 100 µS/cm (Sadik et al. 2013b). The solution conductivity was measured using a Conductivity/TDS Meter (Oakton, Vernon Hills, IL). The pH of the buffer solution was measured with a Beckman 340 pH/Temp Meter (Beckmann Coulter, Fullerton, CA) and maintained at 7.4. The osmolarity of the solution was measured using the Advanced Osmometer 3D3 (Advanced Instrument, Norwood, MA) and adjusted to a cell compatible level of 310 mOsm/kg.

2.4 Generating non-rotating cells via balanced sheath-flow rates

Non-rotating single-cell movement down the channel was achieved using standard hydrodynamic focusing. The pulsing buffer served as the sheath fluid to sandwich the cell stream and was infused from the two lateral inlets in a three-inlet, three-outlet microchannel at equal flow rates (Fig. 1a). Precision microfluidic syringe pumps (PicoPlus, Harvard Apparatus, Holliston, MA) were used to deliver both the sheath and cell streams at controlled flow rates. While keeping the cell stream at a constant flow rate of 0.5 µL/min, the flow rate of the lateral sheath streams was increased from 0.5 to 4.5 µL/min in increments of 0.5 µL/

min in order to focus the cell stream to the channel center, pinching the cells into a single file.

2.5 Generating rotating cells via differential flow rates

Cell rotation was generated in a two-inlet, two-outlet microchannel (Fig. 1b) using a differential flow-shearing technique. The pulsing buffer was infused from one of the inlets to serve as a sheath to define the width of the pinched cell stream to the channel wall at a relatively higher flow rate, whereas the cells suspended in the pulsing buffer was infused from the other inlet. Flow-rate ratios of 1:1, 2:1, 5:1 and 10:1 between sheath and cell stream were investigated. To evaluate the effects of perfusion flow rate on cell angular velocity, flow rates were varied from 1 to 4.5 μL/min in 0.5 μL/min increments at each flow-rate ratio.

2.6 Intracellular molecular delivery of PI

The locations where biomolecules enter through the permeabilized cell membrane were visualized via the delivery of PI. An initial 20-ms-duration DC pulse was applied to the cells at 0.6 kV/cm electric field strength to sufficiently permeabilize the cell membrane according to our previous work (Sadik et al. 2013b); immediately following a 10 ms delay, another 20-ms-duration DC pulse was applied to demonstrate the cell rotation-mediated permeabilization of (1) the entire circumference of the cell membrane; (2) two distinct membrane locations and (3) a single location for non-rotating cells. All three conditions were achieved for single cells rotating at a fast (8°/ms), slow (5°/ms) and zero angular velocity. The electroporation was activated manually once stable stratified flows had been established. A low density cell suspension (2 million/ml) was used in the hydrodynamically focused flow stream to ensure each cell flowed individually between the electrodes and received the applied electric field. A triggering signal instantly initiated the pulse generator and the camera recorder, allowing all events during and after electroporation to be recorded. The acquired fluorescence images were stored only for cells that remained between the electrodes for the entire duration of the electroporation pulses.

2.7 Intracellular molecular delivery of FD

A continuous electroporation pulsing scheme (Morales et al. 2012) was devised to allow repeated cell membrane permeabilization followed by delivery of macromolecules (FD) into rotating and non-rotating single cells. By collecting the electroporated single cells at the channel outlet and analyzing the cells by pipetting the sample onto a microscope slide for image analysis, delivered payload could be quantified for rotating, non-rotating single cells and a control case. Detailed description of microchannel flow operation and electroporation pulse parameters can be found in the supplemental file part A.

2.8 Image capture and processing

Bright-field images of flowing single cells were captured using a CMOS multimodal camera (PCO.Edge.4.2, PCO-TECH, Londonderry, NH) under the rolling shutter mode at a capture frequency of 2000 frames per second in conjunction with a 0.5-ms exposure. Cellular surface features were used to determine rotational velocity, so cell features such as shape and cytoplasmic structures needed to be visibly identifiable. This was achieved geometrically by reducing the height of the microchannel to 20 μm to ensure that all cells were in focus and optically by setting the microscope to a differential-interference-contrast (DIC) mode. A total of 1000 time-stamped images were collected for each cell.

To assess small-molecule (PI) delivery during electroporation, the same CMOS camera was operated in epifluorescence mode to capture fluorescent images at 2000 frames per second with a 0.5-ms exposure time in separate experiments. The camera was synchronized with the electroporation pulse generator to permit instantaneous activation of optical recording and electroporation with negligible delay (<1 ns). The applied electric field strength, duration, frequency and shape were verified with a 54600B model oscilloscope (Hewlett Packard, Palo Alto, CA). All raw images and data were collected and analyzed using MATLAB (The Mathworks, Natick, MA). To account for background noise, four corners of each image with a dimension of 20 × 20 pixels, where image intensity changes were not observed, was first averaged and then subtracted from each image. The total fluorescence intensity of each cell was calculated by summing the signal over the entire cell volume for each image frame (Sadik et al. 2013a).

To assess large-molecule (FD) delivery after electroporation, cells were first collected at the device outlet and then pipetted onto a glass slide and sealed with a coverslip. An interactive, cell-scanning algorithm was written in MATLAB to allow all single cells to be identified after they were visualized on the slide, and then processed to quantify their fluorescent signals. Briefly, bright-field and epi-fluorescence images of the target cells were both captured by the CMOS camera and processed jointly by the MATLAB detection algorithm. The bright-field images allow accurate scanning and labeling of each cell due to the high edge contrast under the DIC imaging mode, while epi-fluorescent images overlaid beneath the bright-field images were used for intensity analysis. The location and extent of each identified cell was directly transcribed onto the epi-fluorescent images to ensure accurate measurement of the intensity for each cell's volume only. The user verifies all

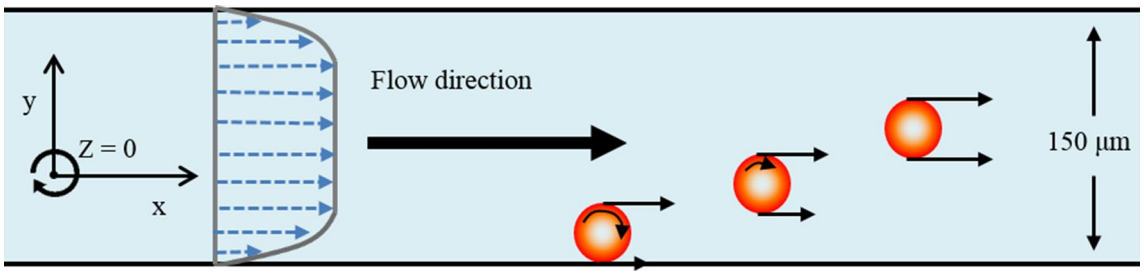

Fig. 2 Schematic drawing of the velocity profile in a microfluidic channel with cells flowing at various distances away from the sidewall. Shear is highest at the wall, while the cell experiences various degrees of rotation depending on its relative position from the wall

images in order to prevent false-positive identification from similar-sized debris or cell fragments.

3 Results and discussion

3.1 Hydrodynamic fluid shearing and cell rotation in a microchannel

Characterization of the microfluidic channel under fluid perfusion was carried out to better understand the effects of fluid flow on cell rotation. The schematic in Fig. 2 illustrates the flow profile at the channel center plane perpendicular to the depth direction with cells experiencing different velocities across the streamlines near the wall. For notation purposes, the x-axis represents the flow direction, the y-axis extends across the channel width and the z-axis extends in the direction of the channel depth.

In the idealized case of a spherical particle following a simple two-dimensional shear flow (i.e., at a low Reynolds number with torque-free boundary condition at the particle surface), the particle will rotate around the flow vorticity axis (and the particle center) proportional to the local flow rotation rate. The rotation rate, ω, of the particle is directly proportional to the shear rate, $\dot{\gamma}$ as

$$\omega = \frac{\dot{\gamma}}{2} \tag{1}$$

The general situation with non-spherical, ellipsoidal particles at low Reynolds numbers was considered by Jeffery (Jeffery 1922). In this case, the particle rotation is periodic and will rotate about the particle's two polar axes producing Jeffery orbits. Bretherton has shown that by integrating the fluid motions equations described by Jeffery (Bretherton 1962), the rotation rate can be determined through the period of rotation that a particle revolves about the minor axis (Leal and Hinch 1971) as

$$\omega = \frac{2\pi}{T}, \quad T = \frac{2\pi}{\dot{\gamma}}\left(r_e + \frac{1}{r_e}\right) \tag{2}$$

This relationship provides an angular frequency that takes into account the variability in cell shape represented mathematically by an effective axis ratio r_e of the particle, α/β, where α and β are the semidiameters measured parallel and perpendicular to the axis of rotation. For our experiments, we assume our cells to be of spheroids with an effective axis ratio of 1 since the degree of non-sphericity in cell shape is rather small (i.e., a 10 % increase in r_e results in <1 % increase in ω). With the assumption of r_e being 1, the angular frequency ω of Eq. (2) reduces to the particle rotation rate determined in Eq. (1).

The rotation rate depends on shear rate, which is a function of the infused fluid flow rate, the location of cells within the flow channel, as well as the particular channel geometry. For a single cell suspended in buffer under uniform shear rate, $\dot{\gamma}$, in a one-dimensional flow, the fluid's rate of velocity change is normal to the direction of flow at a distance y away from the wall boundary (Leal and Hinch 1971). The shear rate equals zero ($\dot{\gamma} = 0$) when all cells are flowing at the same velocity within parallel streamlines and becomes nonzero in the presence of shear as the flow velocity varies across the streamlines.

We analytically calculate the one-dimensional flow profile within the channel as a function of distance across the channel. The flow is expected to be parabolic in the depth-wise (z) direction. Across the width (y) of the channel, the lateral walls will create a wall boundary layer with a uniform core velocity at any depth. Following similar microchannel characterization studies (Shrewsbury et al. 2001), velocity and shear stress profiles of a Newtonian fluid of viscosity η flowing in a microfluidic channel with a known cross-sectional dimension of 150 µm × 20 µm are plotted at the depth-wise centerline ($z = 0$ plane) in Fig. 3a according to the exact solutions to Stokes equation for the channel geometry (White 1974). The fully developed solutions for axial velocity, $u(y, z)$, and flow rate, Q, can be represented in terms of the pressure gradient dP/dx, solution viscosity and channel geometry as shown in Eqs. (3) and (4):

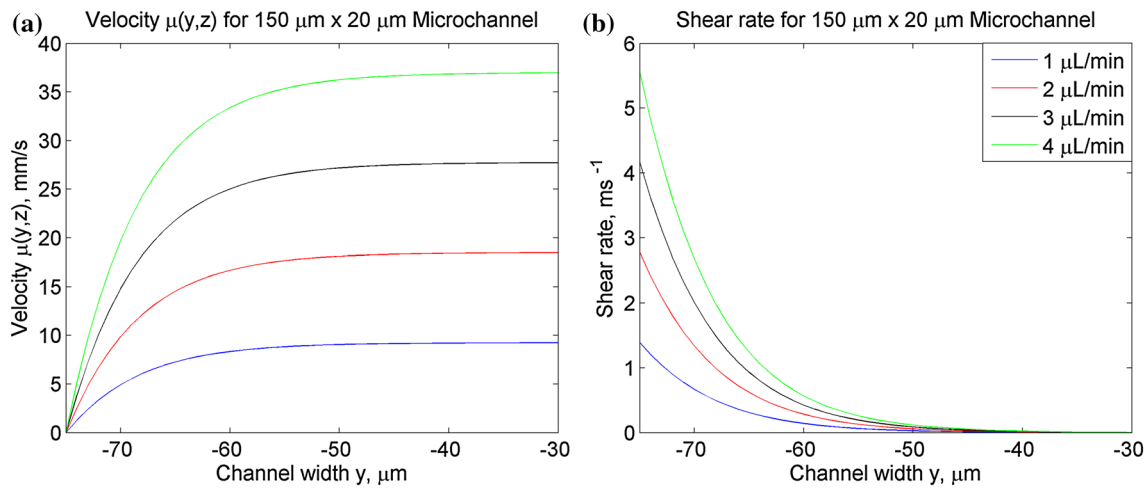

Fig. 3 Fully developed **a** velocity and **b** shear rate profile in a rectangular microfluidic channel at the center plane ($z = 0$), calculated from Eqs. (3) and (5)

$$u(y,z) = \frac{16a^2}{\eta\pi^3}\left(-\frac{\mathrm{d}P}{\mathrm{d}x}\right)\sum_{i=1,3,5\ldots}^{\infty}(-1)^{\frac{i-1}{2}}\left[1-\frac{\cosh\left(\frac{iy}{2a}\right)}{\cosh\left(\frac{ib}{2a}\right)}\right]\cos\left(\frac{i\pi z}{2a}\right)/i^3, \tag{3}$$

$$Q = \left(\frac{4ba^3}{3\eta}\right)\left(-\frac{\mathrm{d}p}{\mathrm{d}x}\right)\left(\left[1-\frac{192a}{\pi^5 b}\sum_{i=1,3,5\ldots}^{\infty}\left[\frac{\tanh\left(\frac{i\pi b}{2a}\right)}{i^5}\right]\right]\right). \tag{4}$$

Briefly, i is an odd integer for the series solution, the solution is valid over the bounds of $-b < y < b$ and $-a < z < a$, where b is the channel half-width and a is the channel half-depth. The shear rate $\dot{\gamma}$ can be determined by taking the derivative of the axial velocity with respect to y assuming the cell is on the center plane ($z = 0$),

$$\dot{\gamma} = \left.\frac{\partial u(y,z)}{\partial y}\right|_{z=0} = \frac{16a^2}{\eta\pi^3}\left(-\frac{\mathrm{d}P}{\mathrm{d}x}\right)\sum_{i=1,3,5\ldots}^{\infty}(-1)^{\frac{i-1}{2}}\left[-\left(\frac{i\pi}{2a}\right)\frac{\sinh\left(\frac{i\pi y}{2a}\right)}{\cosh\left(\frac{i\pi b}{2a}\right)}\right]\left(\frac{1}{i^3}\right). \tag{5}$$

The resultant plot is shown in Fig. 3b. For the channel width of 150 μm, the highest velocity occurs in the center of the channel and is constant across a 60-μm width extending both left and right. The flow profile is also parabolic in the depth-wise direction. For our analysis, the cells were assumed to travel on the depth-wise center plane due to the shallow channel depth (20 μm) so the rotation is exclusively due to vorticity in the z-direction. Experimentally, we found that the cells rotate about the z-axis without any forward tumbling from rotation about the y-axis, validating this assumption. The greatest shear rate occurs at the lateral sidewalls where the flow velocity decreases because of the influence of the bounding walls of the channel.

Closer examination of the fluid shearing motion acting on the cell can reveal how it translates into effective cell rotation. When a single-cell flows close to the channel walls, in the presence of the velocity gradient, two different sides of the cell experience a different velocity depending on the diameter and position of the cell relative to the wall. The shear vorticity is maximal at the walls of the channel where the shear is the greatest so cells within this boundary layer experiences rotation due to the shear gradient. For instance, when the centroid of a 10-μm-diameter cell is positioned 10 μm from the wall during a 4-μL/min fluid perfusion rate, the cell's edge closest to the wall ($y = 5$ μm) would experience a velocity of 20 mm/s, whereas the cell's edge furthest from the wall ($y = 15$ μm) would experience a velocity of 34 mm/s; the velocity differential therefore rotates the cell in a counterclockwise direction. Based on the tendency of a suspended cell to rotate along its vorticity axis, we believe that perfusing the sheath stream can create controllable cell rotations by hydrodynamically pinching the cell stream at prescribed velocities against the channel wall in the x–y plane.

However, the analyses performed by Jeffery assumed an isolated particle within a linear shear flow. In our system, the flow shear rate determined by Eq. (5) is not a linear shear flow. The particle can disrupt the flow profile as the fluid flows around the particle, and friction on the particle can adversely affect the translation of the fluidic shear into rotational torque due to the lateral bounds as well as top

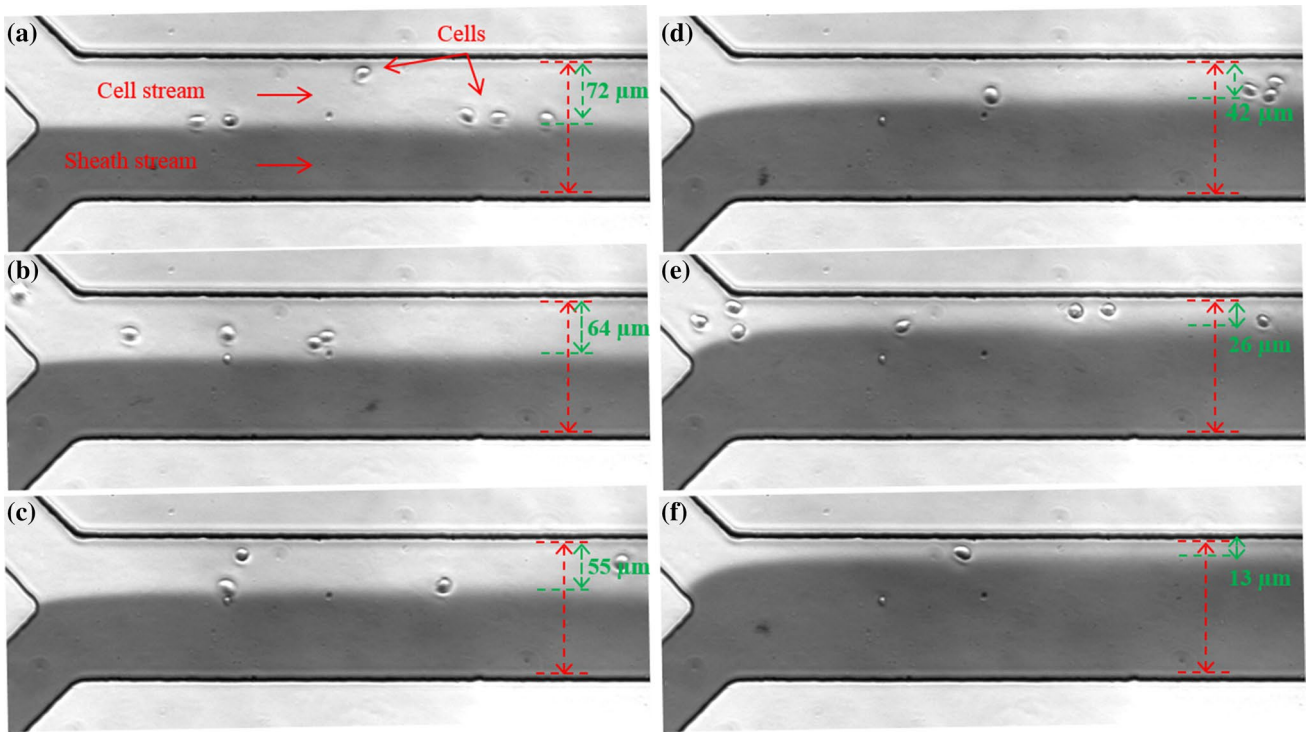

Fig. 4 Hydrodyanmic patterning of the cell stream by a sheathing stream labeled with green dye at 1 µL/min flow rate. The sheath stream increasingly pinches the width of the cell stream which is set to **a** 1 **b** 0.8 **c** 0.6 **d** 0.4 **e** 0.2 and **f** 0.1 µL/min. As a result, the measured width of cell-carrying buffer reduces from (1) 72 to (2) 64 (3) 55 (4) 42 (5) 25 (6) 13 µm

and bottom channel walls. We recognize that complex cell rotation behavior could arise when a particle rotates near the boundaries due to viscous interactions between the fluid, particle and walls; these wall effects on the rotating cells are amplified by three bounding walls of the channel. The effect of channel boundaries on the rotation rate of rigid particle having a fixed radius has been studied in detail with varying particle-wall gaps in the low-Reynolds-number regime (Goldman et al. 1967; Liu and Prosperetti 2010) where the rotation rate decreases logarithmically as the particle edge approaches a bounding wall. Since we pinch the cells to the sidewall in our experiments, a correction factor was determined to account for the aggregating wall effects under hydrodynamic rotation. With the correlation factor, we obtain good agreement between our measured rotation rates and total flow rate.

3.2 Experimental cell rotation

Figure 4 demonstrates the hydrodynamic control of a cell-stream width (top: clear solution with cells) via a sheath buffer (bottom: green dye-labeled buffer). Depending on the flow-rate ratio between the two streams, a tailorable cell-stream width between 13 and 72 µm was achieved as the cell-stream flow rate was varied from 0.1 to 1 µL/min while keeping the sheath-stream flow-rate constant at 1 µL/min to produce a sheathing/cell-stream flow-rate ratio of 10:1–1:1. Cells are more efficiently pinched to the sidewall as the flow-rate ratio increases. Representative longitudinal cell rotation in a counterclockwise direction at different flow rates and flow-rate ratios is demonstrated in Fig. 5. The rotation rate was determined by tracking a constant cell feature from the acquired DIC images such as shape or cytoplasmic structure (marked by arrows) at the periphery of the cell over a period of 80 ms to ensure accuracy of the angular velocity measurement.

Cell angular velocity (ω) can be controlled by the flow-rate ratio between the cell (Q_{cell}) and the sheath-stream flow rates (Q_{sheath}) and the total flow rate ($Q_{cell} + Q_{sheath}$). As demonstrated in Fig. 5a, b, Q_{cell} was maintained at 0.1 µL/min while Q_{sheath} was varied from 0.2 to 0.5 µL/min to obtain an increase in flow-rate ratio from 2:1 to 5:1. This resulted in an increase in ω from 0.4 to 0.8°/ms, respectively. Cell angular velocity can also vary with increasing flow rates while maintaining the same flow-rate ratio between Q_{cell} and Q_{sheath}. Figure 5c, d demonstrates that at a flow-rate ratio of 10:1, doubling Q_{sheath} from 2 to 4 µL/min and Q_{cell} from 0.2 to 0.4 µL/min results in an increase in ω from 2.3 to 4.1°/ms, approximately doubling the rotation rate as well. These results indicate that both the flow-rate ratio and flow rates affect the cell angular velocity. In order to compare the measured rotation

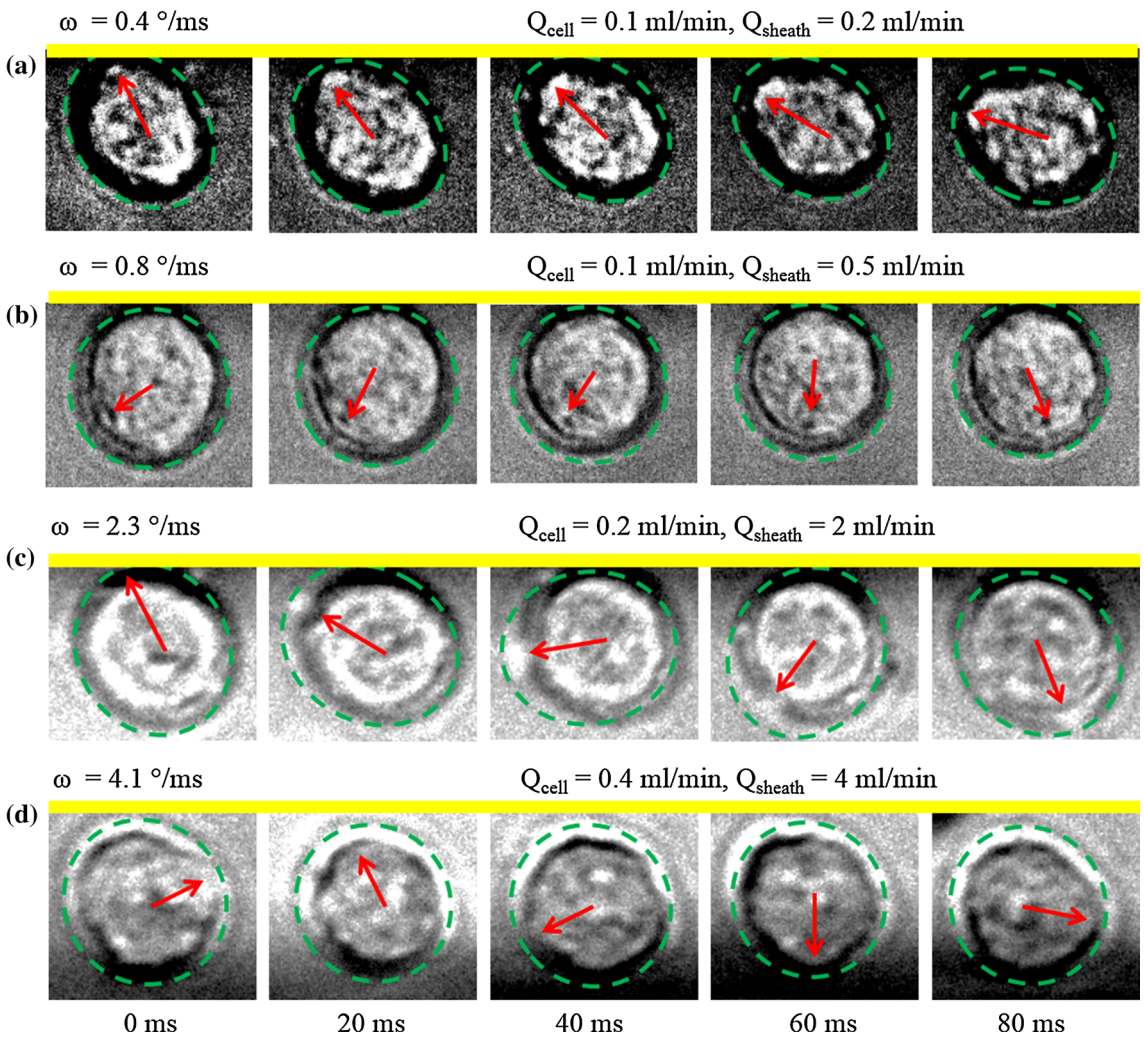

Fig. 5 Differential interference contrast microscopy (DICM) images showing four single cells perfused from left to right, rolling at four angular velocities using four sets of sheathing flow rates and flow-rate ratios

rate to that predicted by Eq. (1), experimental evaluations of 240 cells were carried out to measure the cell angular velocity as a function of both the flow-rate ratio and total flow rates (Fig. 6). Figure 6a shows that even at the lowest flow rate (1 μL/min), increasingly greater cell rotation can be observed with increasing flow-rate ratio, albeit this dependence is small due to the small shear rate. The higher flow-rate ratios elicit a greater and more reliable angular rotation since all cells are pinched closer to the sidewall. However, at lower flow-rate ratios (<10:1), cells in the cell stream are not completely pinched to the channel sidewall but are distributed across the stream width. As a result, cells further from the wall experience a lower average fluidic shear. In addition, cell margination at higher flow rates can further enhance the cell's movement away from the channel wall. A cell-free layer tends to form close to boundaries due to a cell's propensity to marginate toward an area of low shear (Fahraeus and Lindqvist 1931). In these cases, cells that migrate away from the channel wall will experience less rotation. As the sheath-flow rate is increased, the degree of cell rotation can be greatly enhanced as a result of the increased shear rate. While maintaining a flow-rate ratio of 10:1 between the sheath and cell streams, the cell rotation rate was plotted as a function of increasing total flow rate (black curve) (Fig. 6b). There was a linear dependence between the cell rotation rate (within error bars) and flow rate. Thus, the rotation rate can be easily adjusted simply by increasing the total flow rate while maintaining a constant flow-rate ratio of 10:1.

Since the angular velocity of cell rotation is directly proportional to the shear rate of the fluid, a direct link to control the cell rotation through the sheath-flow velocity (flow rate) can be established. The 3T3 fibroblasts used in

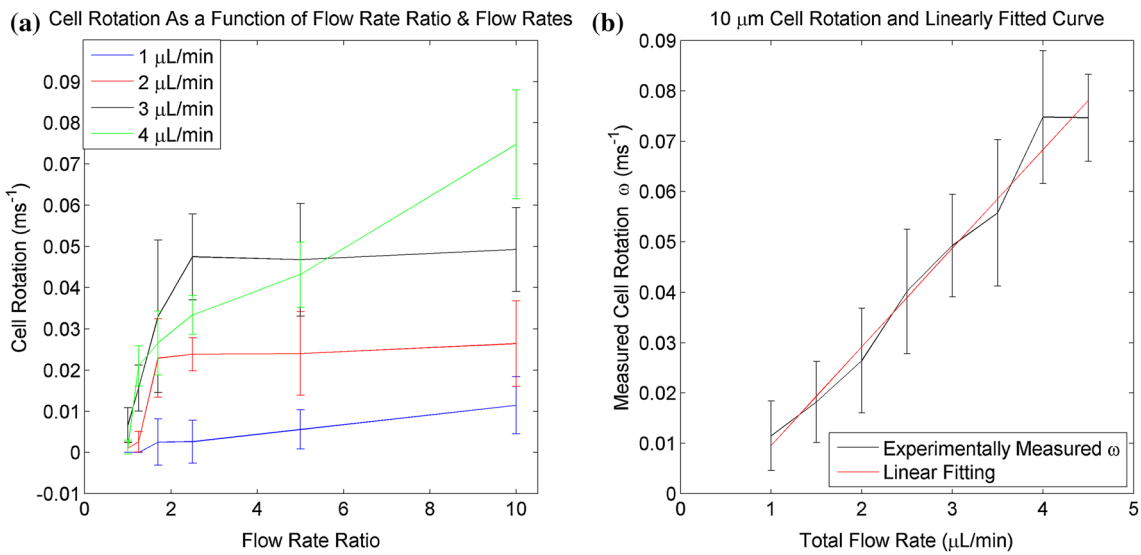

Fig. 6 **a** Measured cell angular velocities as a function of sheath-flow-rate ratios at various flow rates. **b** Cell angular velocities experimentally measured at fixed flow-rate ratio of 10 (*black curve*) and linearly fitted curve (*red curve*)

the experiments have an average diameter of 10 μm, and since they were pinched hydrodynamically to the channel wall, the resultant angular rotation was compared to the shear vorticity estimated within an 8- to 10-μm distance of boundary shearing layer. The measured rotation rate was 4.5 % of the rotation rate predicted by Eq. (1). This discrepancy was attributed to wall effects (Goldman et al. 1967) and wall frictional forces from the boundaries acting on the cell. (Vahidkhah et al. 2014) observed similar discrepancy in their simulation to quantify the tumbling frequency of platelets in the presence and absence of whole blood. For isolated platelets tumbling close to the channel sidewall under linear shear flow in a single-bounding wall, its tumbling frequency is 10 % compared to the platelets far away from the wall in a cell-free layer (Vahidkhah et al. 2014). Additionally, in our experiments, not all cells were perfectly pinched to the channel sidewall due to an irregular cell shape or natural cell drift. Thus, since shear rate decreases rapidly with distance from the wall, the rotation rate of cells located away from the wall would be expected to decrease as well.

3.3 Intracellular molecular delivery of PI under rotating and non-rotating conditions

Two rotating conditions were carried out to demonstrate a difference in PI delivery profiles into rotating cells under the same two-pulse electroporation protocol. When single cells reach the electroporation zone, the first of the two electroporation pulses permeabilizes the cell membrane region perpendicular to the direction of the electric field. The positively charged nucleic acid-binding PI molecules are electrophoretically transported into the cell one pole of the cell. Once the PI enters the cytoplasm, it binds cytosolic nucleic acids and fluoresces. Keeping the pulsing parameters constant (two 20-ms-duration pulses at 0.6 kV/cm *E*-field strength with a 10-ms delay in between), the first rotating condition was generated by a larger Q_{sheath}-to-Q_{cell} ratio, to yield an angular rotation of about 8°/ms (Fig. 7a). At this rotational velocity, a total of 50 ms pulse time would render a 400-cell rotation, which is sufficient to electroporate the entire circumference of the cell. A slight unelectroporated region toward the end of the second pulse was due to the fact that during the initial pulse field it takes some time to permeabilize the cell membrane prior to the observation of PI delivery. The second condition utilized a lower flow rate and smaller Q_{sheath}-to-Q_{cell} ratio to demonstrate a smaller cell angular velocity that would results in incomplete circumferential delivery of PI. At 5°/ms, a total pulse time of 50 ms would render a 250-cell rotation. Figure 7b shows the incomplete circumferential delivery of PI into single cell.

In the non-rotating condition, hydrodynamic focusing was used to balance the cell stream with two sheathing buffer streams so cells flow through the device without rotation. In this condition, the cells reach the electroporation zone and the first pulse permeabilizes the cell membrane and delivers PI into the cell. Then, the second pulse was applied which will further deliver PI at the same membrane location. Due to the saturation of PI during the first delivery pulse, the additional pulse application provides limited increase in intracellular delivery compared to the

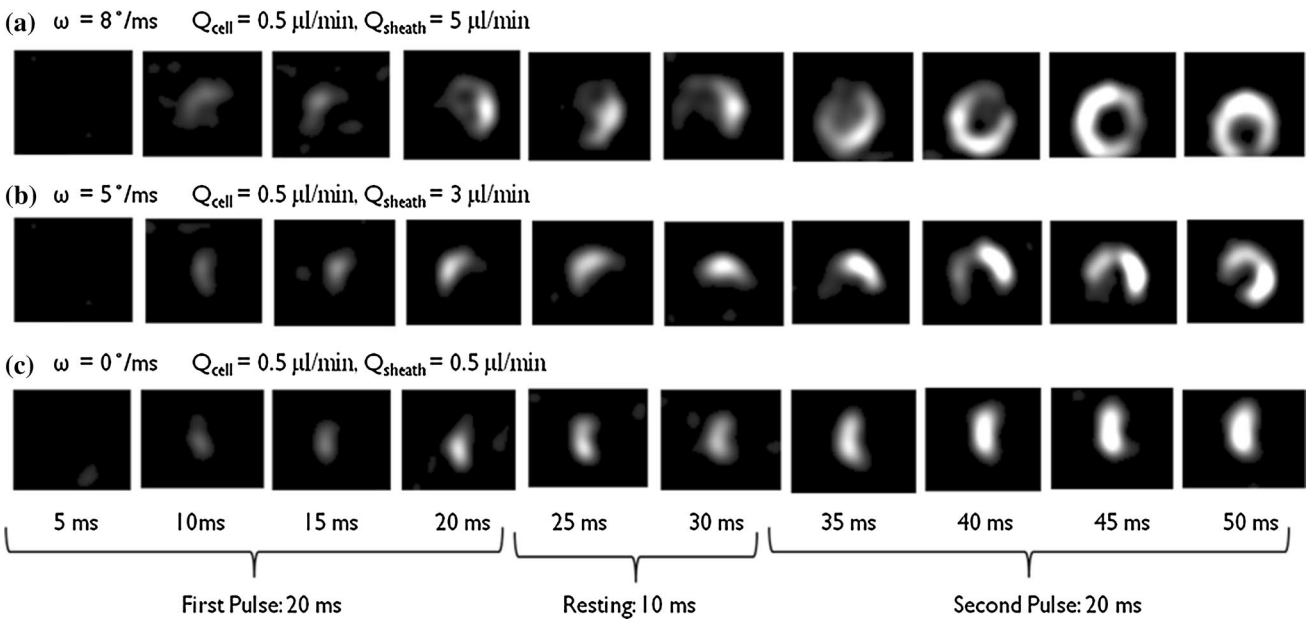

Fig. 7 Spatial and temporal progression of PI delivery into rolling single cell during two-pulse electroporation. The cells flow from *left* to *right* with a clockwise rolling velocity of **a** 8°/ms, **b** 5°/ms and **c** 0°/ms. The first pulse was applied in the first 20 ms, after a 10-ms time delay

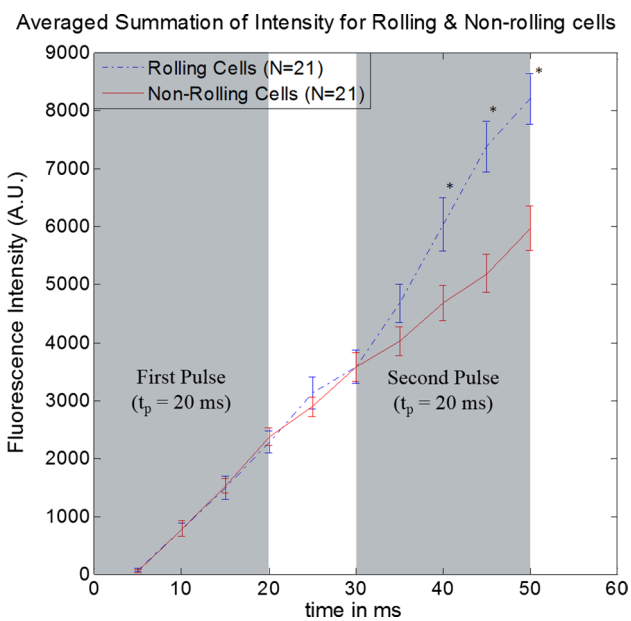

Fig. 8 Total delivered PI intensity with standard error is plotted as a function of time for both rotating and non-rotating cells

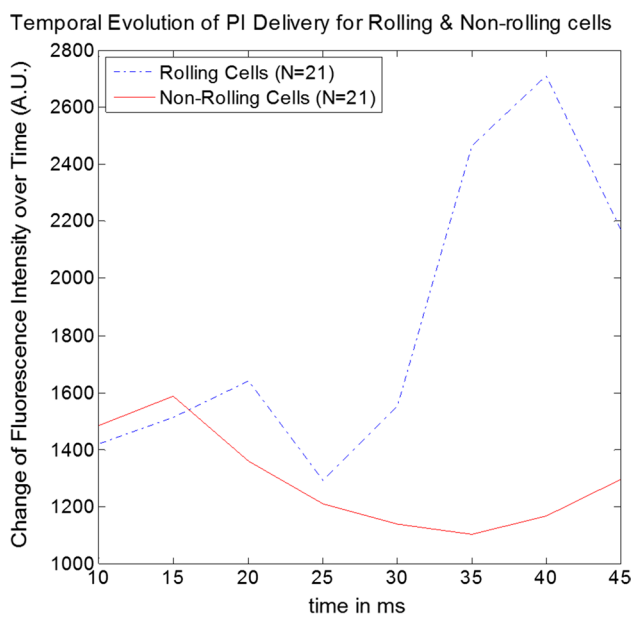

Fig. 9 Finite difference of the intensity between three images at different times was used to estimate the temporal rate of PI delivery plotted according to data in Fig. 4a for both rotating and non-rotating cells

rolling cells. Figure 7c shows the spatial and temporal delivery of PI into single cells permeabilized by electroporation under the non-rotating condition, with both sheath and cell streams perfused at a constant flow rate of 0.5 μL/min.

To further quantify delivery, the fluorescence intensity was summed and compared over the cell image area for both rotation- and non-rotation-mediated PI delivery (Fig. 8). An averaged ($n = 21$ cells) summation of PI delivery intensity with standard error is plotted as a function of time for both rotating (blue curve) and non-rotating (red curve) cells. The gray shading in Fig. 8 indicates the application of the electric field. The intensity of both curves

remains similar during the first 20-ms pulse application. After a 10-ms time delay, the application of a second 20-ms pulse yielded higher fluorescence intensity for rotating cells than for non-rotating cells. A two-sample *t* test showed that the difference between the two curves after 35 ms is significant ($p < 0.05$). The temporal rate of PI delivery was estimated using the finite difference of the intensity between 3 successive images (Fig. 9) for both rotating (8°/ms, blue curve) and non-rotating (red curve) cells. A higher PI delivery rate is apparent for rotation-mediated electroporation during the application of the second pulse when rotation of the cell results in circumferential exposure of the cell membrane to the electric field. As a result, this rotation technique increases not only the rate and amount of delivery but also the delivery profile so that a greater PI delivery payload is obtained throughout the cell volume.

3.4 Intracellular molecular delivery of FD under non-rotating and rotating conditions

To confirm our findings with a larger molecule, we also investigated continuous electroporation of single cells inside the microfluidic channel with predefined pulse parameters to transport FD inside the cells under both rotating and non-rotating conditions. The delivery concentration of FD was quantified based on the fluorescence intensity of the cells collected after perfusion through the microchannel, as presented in Fig. S2. The results demonstrate that cell rotation indeed could augment the intracellular delivery concentration of FD. A detailed explanation can be found in supplemental file part B.

4 Conclusions

This work demonstrates the control of cell orientation via the use of hydrodynamic flows in a microfluidic channel. By combining hydrodynamic flow control-based single-cell rotation with on-chip single-cell microelectroporation, the efficient intracellular molecular delivery of both small (PI) and large (FD) molecules was demonstrated. We show that rotation of the single cells enhances delivery of small molecules compared to standard delivery techniques. Furthermore, by incorporating a continuous pulsing scheme to allow continuous application of electroporating electric field to single cells, large cell populations can be treated and collected for fluorescence intensity analysis. This integration of controlled microfluidic manipulation with a microscale electroporation approach provides a novel paradigm to improve electroporation-mediated transfection. Future work will include an assessment of cell viability and the transfection of large and diverse molecules such as DNA, vesicles. The described technique also enables the development of autonomous microdevices capable of delivering various biological materials and drugs to cells effectively and in a high-throughput manner.

Acknowledgments The authors would like to acknowledge financial support by the National Science Foundation (NSF CBET 0967598, DBI IDBR 1353918)

References

Andersson H, van den Berg A (2003) Microfluidic devices for cellomics: a review. Sens Actuators B Chem 92:315–325. doi:10.1016/S0925-4005(03)00266-1

Bretherton FP (1962) The motion of rigid particles in a shear flow at low Reynolds number. J Fluid Mech 14:284–304

Chiu DT (2007) Cellular manipulations in microvortices. Anal Bioanal Chem 387:17–20. doi:10.1007/s00216-006-0611-2

Demiryurek Y, Nickaeen M, Zheng M et al (2015) Transport, resealing, and re-poration dynamics of two-pulse electroporation-mediated molecular delivery. Biochim Biophys Acta—Biomembr 1848:1706–1714

Di Carlo D, Irimia D, Tompkins RG, Toner M (2007) Continuous inertial focusing, ordering, and separation of particles in microchannels. Proc Natl Acad Sci USA 104:18892–18897. doi:10.1073/pnas.0704958104

Dittrich PS, Manz A (2006) Lab-on-a-chip: microfluidics in drug discovery. Nat Rev Drug Discov 5:210–218. doi:10.1038/nrd1985

Fahraeus R, Lindqvist T (1931) The viscosity of the blood in narrow capillary tubes. Am J Physiol 8:562–568

Gehl J (2003) Electroporation: theory and methods, perspectives for drug delivery, gene therapy and research. Acta Physiol Scand 177:437–447. doi:10.1046/j.1365-201X.2003.01093.x

Goldman AJ, Cox RG, Brenner H (1967) Slow viscous motion of a sphere parallel to a plane wall—I Motion through a quiescent fluid. Chem Eng Sci 22:637–651. doi:10.1016/0009-2509(67)80047-2

Golzio M, Teissie J, Rols M-P (2002) Direct visualization at the single-cell level of electrically mediated gene delivery. Proc Natl Acad Sci USA 99:1292–1297. doi:10.1073/pnas.022646499

Hur SC, Henderson-MacLennan NK, McCabe ERB, Di Carlo D (2011) Deformability-based cell classification and enrichment using inertial microfluidics. Lab Chip 11:912–920. doi:10.1039/c0lc00595a

Jeffery GB (1922) The motion of ellipsoidal particles immersed in a viscous fluid. Proc R Soc A Math Phys Eng Sci 102:161–179. doi:10.1098/rspa.1922.0078

Jons TB (2003) Basic theory of dielectrophoresis and electroporation. IEEE Eng Med Biol 22:33–42. doi:10.1109/MEMB.2003.1304999

Khine M, Lau A, Ionescu-Zanetti C et al (2005) A single cell electroporation chip. Lab Chip 5:38–43. doi:10.1039/b408352k

Khine M, Ionescu-Zanetti C, Blatz A et al (2007) Single-cell electroporation arrays with real-time monitoring and feedback control. Lab Chip 7:457–462. doi:10.1039/b614356c

Kim TK, Eberwine JH (2010) Mammalian cell transfection: the present and the future. Anal Bioanal Chem 397:3173–3178. doi:10.1007/s00216-010-3821-6

Kim JA, Cho K, Shin YS et al (2007) A multi-channel electroporation microchip for gene transfection in mammalian cells. Biosens Bioelectron 22:3273–3277. doi:10.1016/j.bios.2007.02.009

Kim JA, Cho K, Shin MS et al (2008) A novel electroporation method using a capillary and wire-type electrode. Biosens Bioelectron 23:1353–1360. doi:10.1016/j.bios.2007.12.009

Leal LG, Hinch EJ (1971) The effect of weak Brownian rotations on particles in shear flow. J Fluid Mech 46:685. doi:10.1017/S0022112071000788

Lee WG, Bang H, Yun H et al (2008) An impulsive, electropulsation-driven backflow in microchannels during electroporation. Lab Chip 8:224–226. doi:10.1039/b714371k

Li J, Lin H (2011) Numerical simulation of molecular uptake via electroporation. Bioelectrochemistry 82:10–21. doi:10.1016/j.bioelechem.2011.04.006

Li J, Tan W, Yu M, Lin H (2013) The effect of extracellular conductivity on electroporation-mediated molecular delivery. Biochim Biophys Acta—Biomembr 1828:461–470. doi:10.1016/j.bbamem.2012.08.014

Liu Q, Prosperetti A (2010) Wall effects on a rotating sphere. J Fluid Mech 657:1–21. doi:10.1017/S002211201000128X

Mir LM (2000) Therapeutic perspectives of in vivo cell electropermeabilization. Bioelectrochemistry 53:1–10. doi:10.1016/S0302-4598(00)00112-4

Morales MC, Lin H, Zahn JD (2012) Continuous microfluidic DNA and protein trapping and concentration by balancing transverse electrokinetic forces. Lab Chip 12:99–108. doi:10.1039/c1lc20605b

Pamme N (2007) Continuous flow separations in microfluidic devices. Lab Chip 7:1644. doi:10.1039/b712784g

Sadik MM, Li J, Shan JW et al (2013a) Quantification of propidium iodide delivery using millisecond electric pulses: experiments. Biochim Biophys Acta 1828:1322–1328. doi:10.1016/j.bbamem.2013.01.002

Sadik MM, Li J, Shan JW et al (2013b) Quantification of propidium iodide delivery using millisecond electric pulses: experiments. Biochim Biophys Acta—Biomembr 1828:1322–1328. doi:10.1016/j.bbamem.2013.01.002

Schnelle T, Müller T, Reichle C, Fuhr G (2000) Combined dielectrophoretic field cages and laser tweezers for electrorotation. Appl Phys B Lasers Opt 70:267–274. doi:10.1007/s003400050044

Shelby JP, Chiu DT (2004) Controlled rotation of biological micro- and nano-particles in microvortices. Lab Chip 4:168–170. doi:10.1039/b402479f

Shrewsbury PJ, Muller SJ, Liepmann D (2001) Effect of flow on complex biological macromolecules in microfluidic devices. Biomed Microdevices 3:225–238. doi:10.1023/A:1011415414667

Takagi J, Yamada M, Yasuda M, Seki M (2005) Continuous particle separation in a microchannel having asymmetrically arranged multiple branches. Lab Chip 5:778–784. doi:10.1039/b501885d

Vahidkhah K, Diamond SL, Bagchi P (2014) Platelet dynamics in three-dimensional simulation of whole blood. Biophys J 106:2529–2540. doi:10.1016/j.bpj.2014.04.028

White F (1974) Viscous fluid flow, 2nd edn. McGraw-Hill, New York, p 413

Yamada M, Nakashima M, Seki M (2004) Pinched flow fractionation: continuous size separation of particles utilizing a laminar flow profile in a pinched microchannel. Anal Chem 76:5465–5471. doi:10.1021/ac049863r

Yun H, Kim K, Lee WG (2013) Cell manipulation in microfluidics. Biofabrication 5:022001. doi:10.1088/1758-5082/5/2/022001